How to cite: *Angew. Chem. Int. Ed.* **2023,** *62,* e202213228
International Edition: doi.org/10.1002/anie.202213228
German Edition: doi.org/10.1002/ange.202213228

Solid-State Batteries

Impact of the Chlorination of Lithium Argyrodites on the Electrolyte/Cathode Interface in Solid-State Batteries

Tong-Tong Zuo, Felix Walther, Jun Hao Teo, Raffael Rueß, Yubo Wang, Marcus Rohnke, Daniel Schröder, Linda F. Nazar, and Jürgen Janek**

Abstract: Lithium argyrodite-type electrolytes are regarded as promising electrolytes due to their high ionic conductivity and good processability. Chemical modifications to increase ionic conductivity have already been demonstrated, but the influence of these modifications on interfacial stability remains so far unknown. In this work, we study Li_6PS_5Cl and $Li_{5.5}PS_{4.5}Cl_{1.5}$ to investigate the influence of halogenation on the electrochemical decomposition of the solid electrolyte and the chemical degradation mechanism at the cathode interface in depth. Electrochemical measurements, gas analysis and time-of-flight secondary ion mass spectrometry indicate that the $Li_{5.5}PS_{4.5}Cl_{1.5}$ shows pronounced electrochemical decomposition at lower potentials. The chemical reaction at higher voltages leads to more gaseous degradation products, but a lower fraction of solid oxygenated phosphorous and sulfur species. This in turn leads to a decreased interfacial resistance and thus a higher cell performance.

[*] Dr. T.-T. Zuo, Dr. F. Walther, Dr. R. Rueß, Prof. M. Rohnke, Prof. J. Janek
Institute of Physical Chemistry, Justus Liebig University Giessen
Heinrich-Buff-Ring 17, 35392 Giessen (Germany)
and
Center for Materials Research (ZfM/LaMa),
Justus Liebig University Giessen
Heinrich-Buff-Ring 16, 35392 Giessen (Germany)
E-mail: tong-tong.zuo@phys.chemie.uni-giessen.de
juergen.janek@pc.jlug.de

J. H. Teo
Battery and Electrochemistry Laboratory, Institute of Nanotechnology, Karlsruhe Institute of Technology (KIT)
Hermann-von-Helmholtz-Platz 1,
76344 Eggenstein-Leopoldshafen (Germany)

Y. Wang, Prof. L. F. Nazar
Department of Chemistry and the Waterloo Institute for Nanotechnology, University of Waterloo
200 University Avenue West, Waterloo, Ontario N2L 3G1 (Canada)

Prof. D. Schröder
Institute of Energy and Process Systems Engineering (InES), Technische Universität Braunschweig
Langer Kamp 19B, 38106 Braunschweig (Germany)

Introduction

The demand for high energy density and safety accelerates the development of solid-state batteries (SSBs).[1] In order to meet the requirements of high energy and power density, solid electrolytes (SEs) with high ionic conductivity show great potential in satisfying these criteria.[2] Among all SEs, sulfide-based electrolytes exhibit particularly high ionic conductivity and favorable mechanical properties (e.g., high elasticity and ductility), which are important for practical processing of SSBs, especially for thick cathodes. A number of sulfide SEs have been studied including Li_2S-P_2S_5 glasses,[3] $Li_{10}GeP_2S_{12}$,[4] $Li_{9.54}Si_{1.74}P_{1.44}S_{11.7}Cl_{0.3}$,[5] and Li_6PS_5X (X = Cl, Br, I).[6] However, due to the rather limited thermodynamic stability of the thiophosphate and sulfide ions, most thiophosphate SEs exhibit a narrow electrochemical stability window, which is problematic in combination with high voltage cathode active materials (CAMs), such as $LiNi_{1-x-y}Co_xMn_yO_2$ (NCM).[7] Recently, a spate of Li metal halide SEs have been studied intensively, as they provide much better cathode compatibility and high voltage stability, however, their ionic conductivity is still lower than that of optimized sulfide SEs.[8]

Lithium argyrodites with the formula Li_6PS_5X (X = Cl, Br, I) show great advantages owing to their outstanding processability and high ionic conductivity.[9] Kraft et al. systematically studied the influence of the different halide anions (Cl^-, Br^-, and I^-) on the ionic conductivity.[6c] Upon altering the lattice softness of Li argyrodites, the ionic transport was investigated via monitoring the Li^+ occupancy and X^-/S^{2-} site disorder. It was shown that the compositional change of the halide triggers the change of site disorder due to the characteristic properties of different halide anions. Recently, Gautam et al. controlled the site-disorder in Li_6PS_5Br by tuning the synthesis temperature before quenching.[10] The results suggest that a higher degree of site disorder is beneficial for intercage jumps, and leads to a fourfold increase in ionic conductivity to 2 $mS\,cm^{-1}$. Apart from the compositional change of the halide, increasing the halide content from Li_6PS_5Cl to $Li_{5.5}PS_{4.5}Cl_{1.5}$ also introduces more Li^+ vacancies and Cl^-/S^{2-} site disorders.[11] Owing to the weakened interaction between Li ions and the surrounding framework, the Cl-rich argyrodite $Li_{5.5}PS_{4.5}Cl_{1.5}$ shows an enhanced ionic conductivity of 12 $mS\,cm^{-1}$ when pelletized and sintered. Clearly, the ionic conductivity of the Li argyrodites has been greatly improved, but the impact of the chemical modification on the stability and interfacial degra-

dation at the SE|CAM interface has not been studied in depth.

Recently, Dewald et al. and Tan et al. investigated the practical oxidative stability of Li_6PS_5Cl with carbon electrodes.[7b,12] The oxidation of sulfide (S^{2-}) in the thiophosphate polyanions to sulfur (S_x^0 and S_x^{2-} species) dominates the electrochemical decomposition of the SE, representing lithium extraction. However, in contact with the cathode active material (CAM), the formation of oxygenated sulfur and phosphorous species indicates additional chemical degradation at the CAM|SE (e.g., Li_6PS_5Cl|$LiNi_{0.6}Co_{0.2}Mn_{0.2}O_2$) interface.[13] Furthermore, the observation of gaseous products (e.g., SO_2) indicates the reaction between O_2 (presumably singlet $^1O_2$[14]) released from the NCM with Li_6PS_5Cl.[15] These results highlight that both electrochemical decomposition of the SE and its chemical reactivity with the CAM play a critical role and need to be taken into account on the way to optimized interfaces for SSBs.

In this work, we employ Li_6PS_5Cl and $Li_{5.5}PS_{4.5}Cl_{1.5}$ electrolytes as a model system in which the increased halide content affects the ionic conductivity without major structural changes. The electrochemical and chemical stability of the SE is measured in SE/carbon and SE/CAM composite electrodes, respectively. $Li_{5.5}PS_{4.5}Cl_{1.5}$ shows more pronounced decomposition at the interface with both carbon and CAM. Time-of-flight secondary-ion mass spectrometry (ToF-SIMS) and differential electrochemical mass spectrometry (DEMS) were carried out to probe the solid and gaseous degradation products. In comparison with Li_6PS_5Cl, $Li_{5.5}PS_{4.5}Cl_{1.5}$ yields more products containing elemental sulfur (i.e., S_x^0 and polysulfides S_x^{2-}) and more gas (i.e., SO_2), but it forms less solid oxygenated sulfur and phosphorus compounds (i.e., phosphate and sulfate/sulfite). Accordingly, the SE modification leads to changes in the underlying interfacial reactions and thus differences in the fractions of the various cathode|electrolyte interphase (CEI) compounds. A thin and homogeneous lithium phosphate/phosphite or lithium sulfate/sulfite layer in turn improves the cell performance in the case of $Li_{5.5}PS_{4.5}Cl_{1.5}$. Overall, these findings provide new insights into the influence of electrolyte modification on cathode interfacial stability.

Results and Discussion

Li_6PS_5Cl and $Li_{5.5}PS_{4.5}Cl_{1.5}$ electrolytes were prepared by a well-known solid-state synthesis route as reported elsewhere.[11a] Figure S1 shows the XRD patterns of Li_6PS_5Cl and $Li_{5.5}PS_{4.5}Cl_{1.5}$ powders. The reflections at 2θ positions 35° and 50° indicate a very minor LiCl impurity in $Li_{5.5}PS_{4.5}Cl_{1.5}$, while no impurities are found in Li_6PS_5Cl. The ionic conductivity at 25 °C was measured to be 2.9 mS cm^{-1} for Li_6PS_5Cl, whereas $Li_{5.5}PS_{4.5}Cl_{1.5}$ shows a higher conductivity of 7.0 mS cm^{-1}, which is in good agreement with the literature value.[11a]

In order to determine the electrochemical stability window of both SEs, cyclic voltammetry (CV) measurements were performed with carbon electrodes. Figure 1a and b show the CV results of the Li_6PS_5Cl/C and $Li_{5.5}PS_{4.5}Cl_{1.5}$/C electrodes, respectively. At a scan rate of 0.05 mV s^{-1}, the $Li_{5.5}PS_{4.5}Cl_{1.5}$/C electrode exhibits an approximately twofold higher current density compared with the Li_6PS_5Cl/C electrode, while all maxima appear at the same potentials (Figure S2). Under the assumption that both electrolytes are equally well in contact with the carbon, this result indicates that a) $Li_{5.5}PS_{4.5}Cl_{1.5}$ is more susceptible to electrochemical decomposition than Li_6PS_5Cl, and that b) the oxidation mechanism is similar.

The electrochemical decomposition of thiophosphate SEs has been widely investigated experimentally and computationally.[7b,12,16] Theoretically, Li argyrodite Ses decompose first into LiCl, Li_3PS_4 and S (more correctly S_x^0 and/or S_x^{2-}, depending on the degree of oxidation) upon oxidation [Reactions (1) and (2)], subsequently Li_3PS_4 decomposes into S and P_2S_5 after complete oxidation [Reaction (3)].

$$Li_6PS_5Cl \rightarrow LiCl + Li_3PS_4 + S + 2Li^+ + 2e^- \quad (1)$$

$$Li_{5.5}PS_{4.5}Cl_{1.5} \rightarrow 1.5LiCl + Li_3PS_4 + 0.5S + Li^+ + e^- \quad (2)$$

$$Li_3PS_4 \rightarrow 0.5P_2S_5 + 1.5S + 3Li^+ + 3e^- \quad (3)$$

Reactions (1)–(3) are highly simplified as the underlying decomposition processes are mechanistically rather complex, involving a large variation of possible intermediate products (e.g., PS_4^{3-}, $P_2S_7^{4-}$, and $P_2S_6^{2-}$).[7b] However, following these

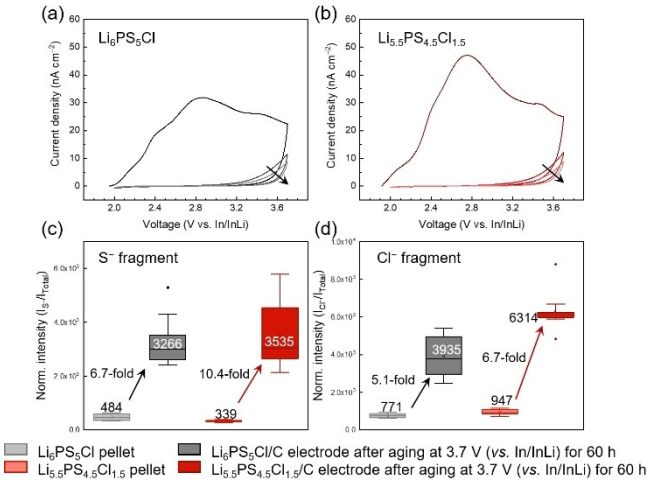

Figure 1. CV measurements of a) In/InLi|Li_6PS_5Cl|Li_6PS_5Cl/C and b) In/InLi|$Li_{5.5}PS_{4.5}Cl_{1.5}$|$Li_{5.5}PS_{4.5}Cl_{1.5}$/C cells at 25 °C. The content of C additive is 20 wt%. The surface area of C65 was measured to be 59 m^2 g^{-1}. We assume that all carbon particles are well covered by SEs in the SE/C electrode. The arrows indicate the CV curves from the first to the third cycle. Box plots of normalized c) S^- and d) Cl^- signal intensities of ToF-SIMS surface analyses (10 measurements per sample) of SE/C electrodes. The signal intensity is normalized to the total ion signal intensity of the corresponding spectrum. The average signal intensities were labelled in (c) and (d). The relative increase of S^- and Cl^- signal intensities were evaluated to compare the decomposition degree of SEs.

equations for sake of simplicity, the complete decomposition process of the SE should involve $5e^-$ per formula unit for Li_6PS_5Cl and $4e^-$ per formula unit for $Li_{5.5}PS_{4.5}Cl_{1.5}$. Consequently, the higher current density in the CV measurements could be explained either by a higher fraction of decomposed SE material or by a "more complete" decomposition process.

In contrast to Li_6PS_5Cl, a lower oxidation onset is found for $Li_{5.5}PS_{4.5}Cl_{1.5}$ (Figure S2). This correlates with its thermodynamically unstable nature determined from differential scanning calorimetry (DSC) and thermal gravimetric analysis (TGA) measurements. In the DSC measurement (Figure S3a), sharp melting/crystallization peaks were observed for Li_6PS_5Cl at 535 °C/532 °C, respectively. For $Li_{5.5}PS_{4.5}Cl_{1.5}$, the melting/crystallization peaks become broader and shift to lower temperature (523 °C/493 °C), which may indicate incongruent melting. The TGA curves show no significant mass loss for Li_6PS_5Cl, but for $Li_{5.5}PS_{4.5}Cl_{1.5}$, the mass starts to drop at 315 °C (Figure S3b). The underlying reactions during heating remain elusive. Nevertheless, both DSC and TGA experiments demonstrate the thermodynamic instability of $Li_{5.5}PS_{4.5}Cl_{1.5}$, which leads to a larger driving force towards decomposition in electrochemical measurements.

The galvanostatic intermittent titration technique (GITT) was applied to investigate the voltage-dependence on the electrochemical decomposition. Upon polarization, the sharp voltage increase (IR drop) reflects the internal resistance in the cell (Figure S4a). In the low voltage range (< 3 V vs. In/InLi), the internal resistance of cells with either Li_6PS_5Cl or $Li_{5.5}PS_{4.5}Cl_{1.5}$ is almost the same, while the $Li_{5.5}PS_{4.5}Cl_{1.5}$/C electrode exhibits higher capacity due to electrochemical decomposition. At voltages above 3 V vs. In/InLi, the internal resistance of the $Li_{5.5}PS_{4.5}Cl_{1.5}$/C electrode increases faster than the Li_6PS_5Cl/C electrode, and the two electrodes deliver similar decomposition capacity. This implies that the electrochemical decomposition is a voltage-dependent process, while it is difficult to correlate the IR drop with decomposition steps due to the lack of detailed compositions and their resistance.

ToF-SIMS measurements were performed on the surface of SE/C electrodes (oriented towards the current collector) after holding the voltage at 3.7 V vs. In/InLi for 60 h. Figure 1c and d show the signal intensities of S^- and Cl^- secondary ions (normalized to the total ion signal intensity) for both SEs, respectively. Under the assumption that S^- and Cl^- are more easily formed from decomposition products (due to higher fragmentation), the strong increase in normalized signal intensities is correlated to the decomposition of both argyrodite materials upon electrochemical oxidation. For Li_6PS_5Cl, the normalized intensity of the S^- signal is similar to $Li_{5.5}PS_{4.5}Cl_{1.5}$ in the pristine pellet as well as after aging. On the contrary, the intensity of the normalized Cl^- signal is higher in the $Li_{5.5}PS_{4.5}Cl_{1.5}$/C electrode after aging. The effect of the current collector on the decomposition reaction is not clear, but this may offset the difference in S^- and Cl^- signal intensities to some extent.[17]

Based on the Reactions (1)–(3), the chemical stoichiometry of the Li argyrodite determines the ratio of the decomposition products. Considering the relative intensity changes of the S^- (6.7- : 10.4-fold increase for Li_6PS_5Cl:$Li_{5.5}PS_{4.5}Cl_{1.5}$) and Cl^- (5.1- : 6.7-fold increase for Li_6PS_5Cl:$Li_{5.5}PS_{4.5}Cl_{1.5}$) signals and the observations on the current density of SE/C electrodes, we speculate that the fraction of decomposition products in the $Li_{5.5}PS_{4.5}Cl_{1.5}$/C electrode is higher than in the Li_6PS_5Cl/C electrode. In other words, $Li_{5.5}PS_{4.5}Cl_{1.5}$ shows a higher degree of electrochemical decomposition.

To quantify the interfacial degradation at the SE|NCM85 interface, Li_6PS_5Cl/NCM85 and $Li_{5.5}PS_{4.5}Cl_{1.5}$/NCM85 cells were charged up to 3.7 V vs. In/InLi and held at this voltage, while impedance spectra were measured every 25 min for 30 h. Figure 2a, b show that the resistance of the two cells increases strongly during aging. A transmission line model (TLM) was applied to extract the charge transfer and the electronic/ionic transport processes in the composite cathodes (Figure 2c).[18] As the impedance shows a typical Gerischer-type behavior, the charge transfer and transport resistances cannot be accurately decoupled from each other by fitting. However, an effective total resistance of the composite cathode can be determined as:[18e]

$$R_{cat} = \sqrt{R_{ct}(R_{el} + R_{ion})} \quad (4)$$

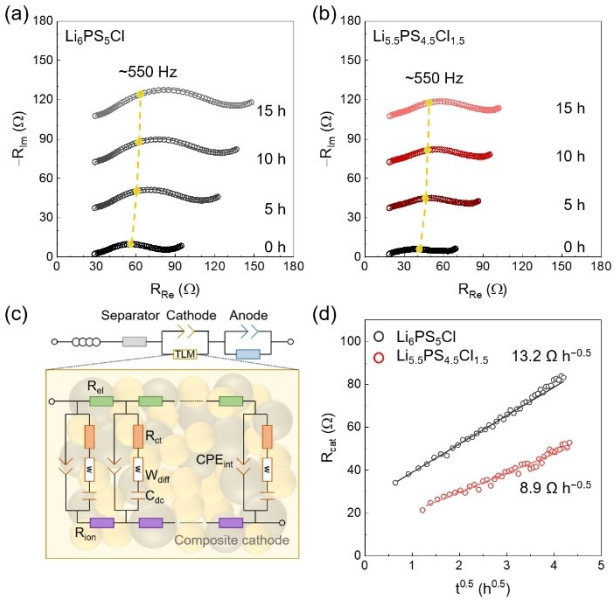

Figure 2. Impedance evolution of a) Li_6PS_5Cl and b) $Li_{5.5}PS_{4.5}Cl_{1.5}$ SSBs resting upon 3.7 V vs. In/InLi at 25 °C. The impedance spectra are stacked with a y-axis shift of 35 Ω for each spectrum. The equivalent circuit and the corresponding contributions are marked in (c). The transport-reaction scheme in the composite cathode is described by a transmission line model (TLM). R_{ct}, R_{el} and R_{ion} represent the resistance contributions from charge transfer, electron transport and ionic transport, respectively. W_{diff} denotes the Warburg impedance for diffusion inside insertion active particle. C_{dc} accounts for the differential capacity of NCM. CPE_{int} represents the constant phase element for the interfacial capacitance. d) Comparison of R_{cat} increase against the square root of time ($t^{0.5}$).

where R_{cat} denotes the overall cathode resistance. R_{ct}, R_{el} and R_{ion} represent the resistance contributions from charge transfer, electron transport and ionic transport, respectively. Figure S5 displays the impedance evolution of the cathode and anode parts. The resistance contribution of the cathode side dominates the total resistance of the cell and increases parabolically over time. As shown in Figure 2d, the resistance of the Li_6PS_5Cl/NCM85 composite cathode exhibits a steep square root increase with a rate constant of $13.2\,\Omega\,h^{-0.5}$. In contrast, the resistance of the $Li_{5.5}PS_{4.5}Cl_{1.5}$/NCM85 cathode increases parabolically with a rate constant of $8.9\,\Omega\,h^{-0.5}$. This result suggests that the interfacial degradation of the $Li_{5.5}PS_{4.5}Cl_{1.5}$/NCM85 composite cathode is slower, and we assume the following mechanism: first, electrochemical decomposition by extraction of lithium and oxidation of sulfur (without contribution of oxygen from the NCM) takes place on the NCM surface, analogous to the SE/C interface. Additionally, a chemical reaction of NCM and the SE can occur, which is probably accompanied by oxygen release from the NCM85 lattice at high voltages (>3.6 V vs. In/InLi). The highly reactive oxygen species can further react with the SE and leads to gaseous and oxygenated degradation products.[7c,19] Therefore, the parabolic increase in resistance shows a combined effect of electrochemical decomposition and chemical degradation.

To monitor the impedance evolution during cycling, full cells with NCM85 and different SEs were examined at $0.96\,mA\,cm^{-2}$ (0.5 C). The Li_6PS_5Cl cell displays an initial charge and discharge capacity of 215 and $165\,mAh\,g^{-1}$ (Figure 3a), while the $Li_{5.5}PS_{4.5}Cl_{1.5}$ cell exhibits an initial charge and discharge capacity of 215 and $170\,mAh\,g^{-1}$ (Figure 3b), resulting in Coulombic efficiencies of 77 % and 79 %, respectively. After 50 cycles, the Li_6PS_5Cl and $Li_{5.5}PS_{4.5}Cl_{1.5}$ cells still show discharge capacities of 133 and $145\,mAh\,g^{-1}$, respectively. After each charging step, impedance spectra was measured and fitted with the equivalent circuit (Figure 2c) to extract the cathode interfacial charge transfer processes in the cells. The increasing resistance during cycling is ascribed to the interfacial reactions at the SE|CAM interface (Figure S6). Upon cycling, the $Li_{5.5}PS_{4.5}Cl_{1.5}$ cell exhibits higher capacity than the Li_6PS_5Cl cell, but the differences in resistance increase of the two cells are insignificant. We note that the cells for the measurements shown in Figure 2 were held at 3.7 V vs. In/InLi—which would support the chemical degradation caused by oxygen release from the NCM85, whilst the electrochemical decomposition would be more pronounced during cell cycling as shown in Figure 3.

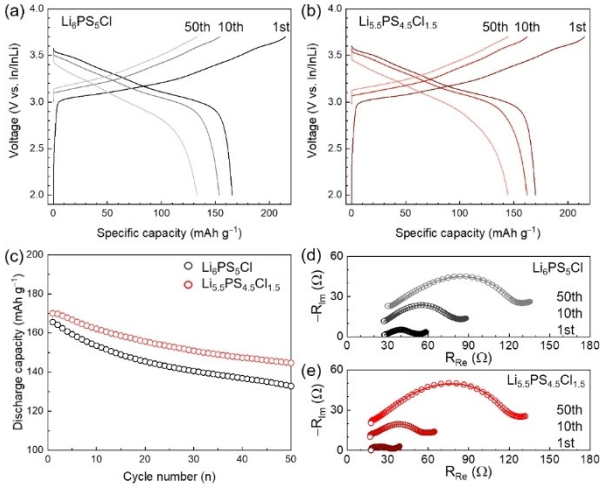

Figure 3. Galvanostatic charge/discharge curves of a) Li_6PS_5Cl and b) $Li_{5.5}PS_{4.5}Cl_{1.5}$ cells at 0.5C. c) Comparison of the cycling stability of two cells. Nyquist plots of d) Li_6PS_5Cl and e) $Li_{5.5}PS_{4.5}Cl_{1.5}$ cells after 1st, 10th and 50th charge.

In addition, the morphological/structural degradation is typically more pronounced at higher cycle numbers. Assuming that the mechanical properties of both SEs are similar, morphological/structural degradation should be more or less comparable for both SSBs and should therefore contribute to a similar extent to the overall SSB performance at higher cycle numbers.

Given the different ionic conductivity for the different Li argyrodites, the transport kinetics in two composite cathodes were compared by rate experiments. As shown in Figure S5a,b, Li_6PS_5Cl and $Li_{5.5}PS_{4.5}Cl_{1.5}$ cells show initial discharge capacities of 183 and $198\,mAh\,g^{-1}$ at 0.1 C, respectively. With increasing C-rate, the Li_6PS_5Cl cell exhibits gradually decaying discharge capacities of 165, 132, 96, and $46\,mAh\,g^{-1}$ at 0.2, 0.5, 1 and 2 C, respectively. In contrast, the $Li_{5.5}PS_{4.5}Cl_{1.5}$ cell displays higher discharge capacities of 185, 160, 132, and $85\,mAh\,g^{-1}$. The obvious difference in rate capability could be ascribed to the higher ionic conductivity of $Li_{5.5}PS_{4.5}Cl_{1.5}$. On the one hand, the $Li_{5.5}PS_{4.5}Cl_{1.5}$ separator facilitates ion transport between electrodes with lower overvoltage. On the other hand, $Li_{5.5}PS_{4.5}Cl_{1.5}$ offers a higher local ionic conductivity in the composite cathode. In order to deconvolute both contributions to the rate capability, four cells with the following separator|cathode combinations were examined:

Li_6PS_5Cl SE|Li_6PS_5Cl/NCM composite cathode

$Li_{5.5}PS_{4.5}Cl_{1.5}$ SE|Li_6PS_5Cl/NCM composite cathode

Li_6PS_5Cl SE|$Li_{5.5}PS_{4.5}Cl_{1.5}$/NCM composite cathode

$Li_{5.5}PS_{4.5}Cl_{1.5}$ SE|$Li_{5.5}PS_{4.5}Cl_{1.5}$/NCM composite cathode

Figure S8 and Table S1 display the rate capability of the four cells. At low C-rate conditions (0.1 C and 0.2 C), the two cells with $Li_{5.5}PS_{4.5}Cl_{1.5}$/NCM cathodes exhibit higher capacity, while the two cells with $Li_{5.5}PS_{4.5}Cl_{1.5}$ SEs show higher capacities at high C-rates. This implies that the limiting step is rooted in the composite cathode at low C rates, while the ionic conductivity of the SE separator dominates the rate capability at high C-rates. Obviously, the higher ionic conductivity of the $Li_{5.5}PS_{4.5}Cl_{1.5}$ SE is favorable for the construction of SSBs.

In order to investigate the interfacial degradation processes, ToF-SIMS surface analysis was carried out on the

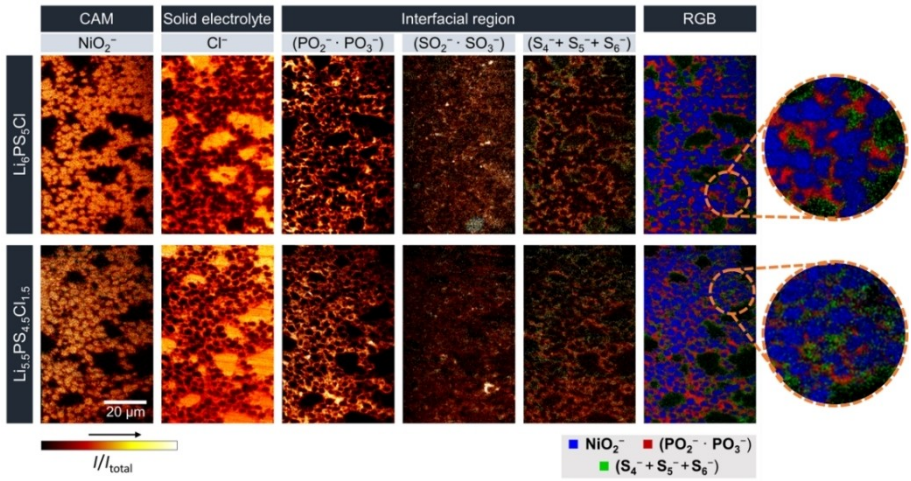

Figure 5. ToF-SIMS measurements of Li_6PS_5Cl/NCM and $Li_{5.5}PS_{4.5}Cl_{1.5}$/NCM cells after 100 cycles. All spectra were measured in negative ion mode on the sidewalls of 45° craters. All secondary ion images were normalized to the total ion signal to compensate topographic effects such as the FIB crater geometry. Exemplary of Supporting Information images of NiO_2^-, Cl^-, $(PO_2^- \cdot PO_3^-)$, $(SO_2^- \cdot SO_3^-)$, $(S_4^- + S_5^- + S_6^-)$ and a RGB overlap. Cathode active material particles, solid electrolyte, and degradation layer are well distinguished in the overlay image.

side of the composite cathode (SE/NCM) that was oriented towards the current collector, after aging for 60 h at 3.7 V. The normalized intensities related to S^- and Cl^- increase strongly during aging for both electrodes (Figure 4a,b), suggesting electrochemical decomposition of both SEs (higher fragmentation of the SE). Assuming the microstructures in the composite cathodes are similar (Figure S9), the comparably higher intensities of the $Li_{5.5}PS_{4.5}Cl_{1.5}$/NCM electrode after aging indicate more severe SE decomposition. Figure S10 presents the signal intensities of a series of polysulfide species (S_x^-, $1 \le x \le 4$). The increase in S^- intensity after aging is reflected as well in the S_2^- and S_3^- signals for the $Li_{5.5}PS_{4.5}Cl_{1.5}$/NCM electrode. However, concerning the overlapping impact of current collectors,[17,20] the difference in two electrodes is gradually eliminated, especially for the S_4^- fragment.

Due to the affinity of oxygen to react with phosphorus and sulfur, phosphate (PO_x^-) and sulfite/sulfate (SO_x^-) fragments are regarded as indicators for oxygen-involving degradation.[13,17,20,21] As shown in Figure 4c, d, in contrast to S_x^- and Cl^- signals, higher normalized intensities for PO_3^- and SO_3^- fragments were observed on the surface of the Li_6PS_5Cl/NCM electrode. This result indicates that less solid oxygenated sulfur and phosphorus species form at the $Li_{5.5}PS_{4.5}Cl_{1.5}$/NCM interface. Below, we propose a mechanism to explain these results in more detail.

In order to verify the above surface analytical results, additional post mortem ToF-SIMS analyses were conducted at 45° FIB crater sidewalls. Figure 5a displays exemplary secondary ion (SI) images of two composite cathodes after 100 cycles. NiO_2^- and Cl^- signals were used to distinguish the cathode active material and the electrolyte particles, respectively. For interfacial degradation, phosphate (PO_x^-), sulfate/sulfite (SO_x^-) and polysulfide (S_x^-) signals represent different degradation processes at the SE|NCM interface. To eliminate the mass interference and maintain the lateral

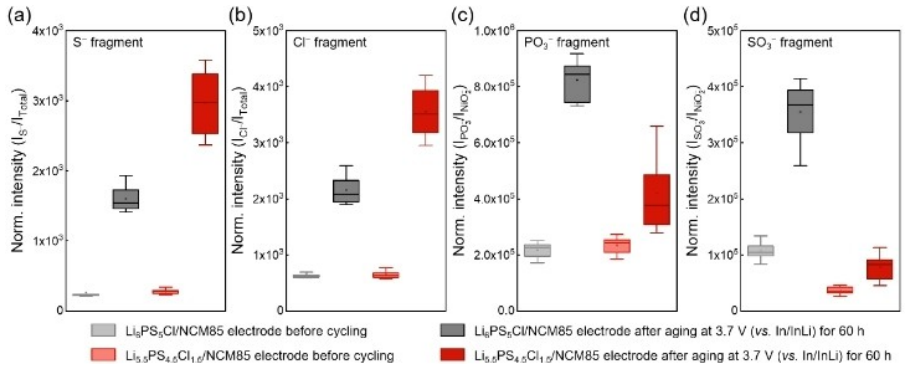

Figure 4. Box plots of normalized a) S^- and b) Cl^- signal intensities from ToF-SIMS surface analyses of SE/NCM85 electrodes after aging at 3.7 V (vs. In/InLi) for 60 h. The signal intensities in (a) and (b) are normalized in relation to the total ion signal intensity of the corresponding spectrum. Because we assume that the oxygen-involving degradation chemical degradation exclusively takes place on the surface of the NCM secondary particles, the signal intensities of PO_3^- and SO_3^- fragments in (c) and (d) are normalized by the NiO_2^- signal intensity of the corresponding spectrum. In this way, deviations due to a different fraction of interfaces within the analysis area are partly compensated.

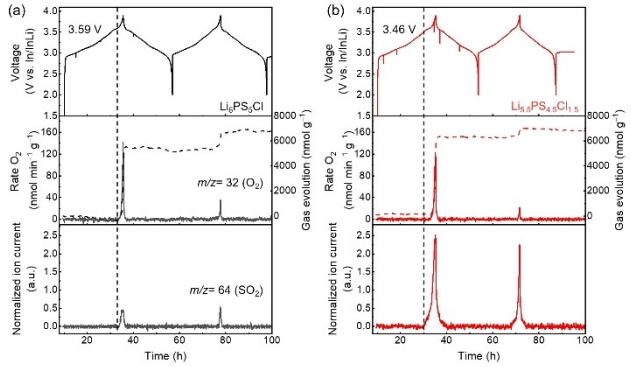

Figure 6. Voltage profile of a) Li_6PS_5Cl and b) $Li_{5.5}PS_{4.5}Cl_{1.5}$ cells cycled at C/20 rate and 45 °C, together with the corresponding time-resolved evolution rate (left *y*-axis) and cumulative gas evolution (right *y*-axis) for O_2 and the normalized ion currents for SO_2.

resolution, PO_x^- and SO_x^- fragments were normalized by multiplication (i.e., $PO_2^-{\cdot}PO_3^-$, $SO_2^-{\cdot}SO_3^-$).[13,20] To enhance the signal intensity of polysulfide fragments (S_x^-), the images of S_4^-, S_5^- and S_6^- were summed (see Supporting Information).

As shown in the overlay RGB image in Figure 5, PO_x^- and SO_x^- products form at the inner degradation layer (close to NCM particles), while S_x^- species form at the outer degradation layer (close to electrolyte particles). In addition to a diffusion-controlled solid-state reaction between the NCM and the SE, oxygen release from the NCM and decomposition of Li_2CO_3 at high voltages (i.e., >4.2 V vs. Li^+/Li) likely cause this inner degradation layer. In contrast, the outer degradation layer is dominated by the electrochemical decomposition reactions of the SEs (i.e., "delithiation"). After long-term cycling, both electrochemical decomposition and chemical degradation contribute to the interfacial resistance, and further voltage polarization.

Figure S11 shows the semi-quantitative results of SIMS crater wall image ROI analysis, which verifies the ToF-SIMS surface analysis shown in Figure 4. Compared with Li_6PS_5Cl, $Li_{5.5}PS_{4.5}Cl_{1.5}$ shows a higher normalized intensity of ($S_4^-+S_5^-+S_6^-$) and a decrease in the normalized intensity of ($PO_2^-{\cdot}PO_3^-$). For ($SO_2^-{\cdot}SO_3^-$); the approximately equal intensities in the two electrodes can be attributed to partially reversible redox behavior of related degradation products.[16c] At the same time, SO_x^- fragments suffer from more pronounced mass interferences with neighboring signals and low signal intensities compared to PO_x^- fragments.

In an attempt to further investigate the oxygen-involving degradation processes at the SE|NCM85 interface, in situ gassing studies via DEMS were performed. The evolved gaseous degradation products could help to elucidate possible degradation mechanisms at the SE|NCM85 interface during cycling. To this end, the cells were cycled at a rate of 0.05 C and 45 °C in the voltage range of 2–3.9 V vs. In/InLi (Figure 6). The Li_6PS_5Cl cell achieved a first cycle charge and discharge capacity of 243 mAh g_{NCM}^{-1} and 201 mAh g_{NCM}^{-1}, respectively. The $Li_{5.5}PS_{4.5}Cl_{1.5}$ cell exhibited a first cycle charge and discharge capacity of 239 and 176 mAh g_{NCM}^{-1}. Note that these two cells were chosen due to their relative similar initial charge capacities. Accordingly, the total amount of gas evolution from both SEs could be compared. The gas evolution was monitored within $m/z=1$–100 and four main gases were detected (H_2 ($m/z=2$), CO_2 ($m/z=44$), O_2 ($m/z=32$) and SO_2 ($m/z=64$)). The evolution of two gases is of major interests in this study, namely of O_2 and SO_2, which will be discussed below. The evolution of H_2 and CO_2 gases is discussed in the Supporting Information (Figure S12).

The O_2 gas evolution ($m/z=32$) is characteristic for layered Ni-rich oxides CAMs. In the case of NCM85, cells are required to achieve a state of charge (SOC) >80 %[19b,22] and this condition is met for both cells with SOC ca. 84.3 % and 82.5 % for the Li_6PS_5Cl and $Li_{5.5}PS_{4.5}Cl_{1.5}$ cell, respectively. The origin of O_2 evolution in layered Ni-rich oxides is a consequence of the destabilization of the crystalline lattice at high voltage (>4.2 V vs. Li^+/Li).[22a,b] Moreover, the amount of O_2 evolved scales exponentially with the lattice destabilization and hence the SOC. With similar charge capacities of the two cells, the cumulative amount of O_2 evolved from both cells is similar (6.7 µmol g_{NCM}^{-1} for the Li_6PS_5Cl cell and 6.8 µmol g_{NCM}^{-1} for the $Li_{5.5}PS_{4.5}Cl_{1.5}$ cell). In addition to the O_2 signal, we monitored the SO_2 gas

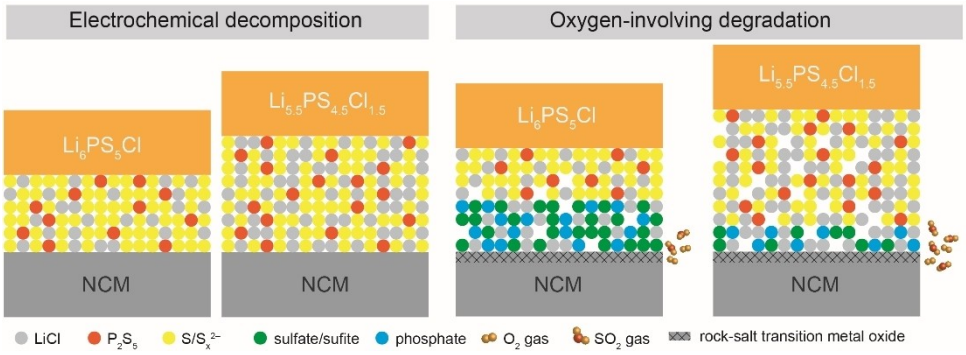

Figure 7. Schematic illustration of SE|NCM interfacial degradation. At low voltages (<4.2 V vs. Li^+/Li), the electrochemical decomposition of Li argyrodites takes place. In the high voltage range (≥4.2 V vs. Li^+/Li), the oxygen-involving degradation dominates the interfacial reactions, and generates gaseous (represented by SO_2) and oxygenated sulfur and phosphorus species (sulfate/sulfite and phosphate) at the interface.

evolution ($m/z = 64$) simultaneously. SO_2 gas evolution is commonly observed for SSB cells containing lithium thiophosphate SEs and indicates oxygen-involving degradation at the SE|CAM interface. Interestingly, the SO_2 gas ion current signal for the $Li_{5.5}PS_{4.5}Cl_{1.5}$ cell had higher intensity compared to the Li_6PS_5Cl cell. This observation suggests that the formation of gaseous products from oxygen-involving degradation is increased for the $Li_{5.5}PS_{4.5}Cl_{1.5}$ cell.[19b,22c,23]

On the basis of the ToF-SIMS and DEMS results, we propose that the oxygen-involving degradation at the SE|CAM interface leads to either gaseous (indicated by SO_2 evolution (DEMS)) or solid products (indicated by PO_x^- and SO_x^- fragments (ToF-SIMS)). The mechanism of interfacial oxygen-involving degradation is rather complex, and the difference in gaseous or solid products remains unclear, which needs further investigation. Modifying the Li argyrodite SEs by halide substitution changes the fraction of gaseous and solid interfacial products which in turn influences the SSB performance.

Upon substitution of S^{2-} with Cl^-, the enhanced Li^+ mobility leads to a higher ionic conductivity for Cl-rich argyrodite. However, the lower thermodynamic stability of $Li_{5.5}PS_{4.5}Cl_{1.5}$ triggers a higher fraction of electrochemical decomposition in SE/C and SE/NCM electrodes (Figure 1 and 4). The oxygen-involving interfacial reactions occur in the high voltage range (≥ 4.2 V vs. Li^+/Li), where the NCM crystal lattice is destabilized and initially inert oxygen ions in the surface layer turn reactive upon oxidation. As a result, interdiffusion and solid-state reactions can occur on the one hand, and highly reactive oxygen species (i.e., singlet oxygen) can be released from the NCM lattice on the other hand, which can then further react with the SE and interfacial species. The oxygen-involving degradation at SE|NCM interface ultimately leads to gaseous species such as SO_2[23] and solid oxygenated phosphorous and sulfur species (e.g., phosphates and sulfates/sulfites).[17,18b] Our results demonstrate that the basic reactions of the different thiophosphate-based SEs with NCM are similar, but the fractions of degradation products are different, which could be attributed to the different stoichiometric ratio of S_x^0, P_2S_5 and LiCl-related species. Accordingly, ToF-SIMS results confirm that $Li_{5.5}PS_{4.5}Cl_{1.5}$ forms less solid oxygenated phosphorous and sulfur species during battery cycling compared to Li_6PS_5Cl. DEMS analysis indicates that $Li_{5.5}PS_{4.5}Cl_{1.5}$ generates more gaseous degradation products such as SO_2 during charging (Figure 7). Future studies may need to investigate the degradation products in more detail. Hence, the thermodynamic and kinetic properties of Li argyrodites play a significant role in driving the SE/CAM interfacial degradation.

Conclusion

In summary, we investigated the influence of argyrodite modification on the interfacial reaction of NCM and SE. For argyrodite modification, the halide content affects the ionic conductivity by introducing Li^+ vacancies and Cl^-/S^{2-} site disorder, while it shows a complex influence on the interfacial degradation in the composite cathodes. $Li_{5.5}PS_{4.5}Cl_{1.5}$ shows a higher fraction of electrochemical decomposition at low voltages compared to Li_6PS_5Cl. At high voltages (i.e., >4.2 V vs. Li^+/Li), $Li_{5.5}PS_{4.5}Cl_{1.5}$ shows a higher fraction of SO_2 gas evolution, but less solid oxygenated phosphorous and sulfur species (e.g., phosphates and sulfates/sulfites). Since the fraction of solid oxygenated degradation products in the interfacial region is reduced, and thus the interfacial resistance is lower, the overall cell performance is enhanced for $Li_{5.5}PS_{4.5}Cl_{1.5}$. By and large, this study shows that the composition and structure of the SE affect the electrochemical decomposition behavior as well as the interfacial reaction between SE and NCM. Thus, new electrolytes, which may in situ form a homogeneous lithium phosphate/phosphite or lithium sulfate/sulfite layer are promising for the modification of new electrolytes. These results highlight the possibility of solving interfacial problems through the targeted modification/development of SEs.

Acknowledgements

This work was supported by the joint project InCa/InCa2 (projects 03XP0228C, 03XP0472A, 03XP0472B) within the German-Japanese cooperation program of BMBF (Federal Ministry for Education and Research) and NEDO (New Energy and Industrial Technology Development Organization), and the projects 03XP0177A and 03XP0430A within the Cluster of Competence FESTBATT funded by BMBF. LFN gratefully acknowledges support from NSERC via a Canada Research Chair and the Discovery Grant program. LFN also acknowledges support through her Liebig professuship at JLU. Open Access funding enabled and organized by Projekt DEAL.

Conflict of Interest

The authors declare no competing financial interests.

Data Availability Statement

The data that support the findings of this study are available from the corresponding author upon reasonable request.

Keywords: Composite Cathode · Interfacial Stability · Lithium Argyrodite Electrolyte · Solid State Battery

[1] a) J. Janek, W. G. Zeier, *Nat. Energy* **2016**, *1*, 16141; b) J. B. Goodenough, Y. Kim, *Chem. Mater.* **2010**, *22*, 587–603; c) A. M. Bates, Y. Preger, L. Torres-Castro, K. L. Harrison, S. J. Harris, J. Hewson, *Joule* **2022**, *6*, 742–755.

[2] a) Y. Kato, S. Hori, R. Kanno, *Adv. Energy Mater.* **2020**, *10*, 2002153; b) K. H. Park, Q. Bai, D. H. Kim, D. Y. Oh, Y. Zhu, Y. Mo, Y. S. Jung, *Adv. Energy Mater.* **2018**, *8*, 1800035; c) S. Xin, Y. You, S. Wang, H.-C. Gao, Y.-X. Yin, Y.-G. Guo, *ACS*

Energy Lett. **2017**, *2*, 1385–1394; d) Y. Zhu, X. He, Y. Mo, *ACS Appl. Mater. Interfaces* **2015**, *7*, 23685–23693.
[3] a) K. Ohara, A. Mitsui, M. Mori, Y. Onodera, S. Shiotani, Y. Koyama, Y. Orikasa, M. Murakami, K. Shimoda, K. Mori, T. Fukunaga, H. Arai, Y. Uchimoto, Z. Ogumi, *Sci. Rep.* **2016**, *6*, 21302; b) F. Mizuno, A. Hayashi, K. Tadanaga, M. Tatsumisago, *Adv. Mater.* **2005**, *17*, 918–921.
[4] a) T. Krauskopf, S. P. Culver, W. G. Zeier, *Chem. Mater.* **2018**, *30*, 1791–1798; b) D. A. Weber, A. Senyshyn, K. S. Weldert, S. Wenzel, W. Zhang, R. Kaiser, S. Berendts, J. Janek, W. G. Zeier, *Chem. Mater.* **2016**, *28*, 5905–5915; c) N. Kamaya, K. Homma, Y. Yamakawa, M. Hirayama, R. Kanno, M. Yonemura, T. Kamiyama, Y. Kato, S. Hama, K. Kawamoto, A. Mitsui, *Nat. Mater.* **2011**, *10*, 682–686.
[5] Y. Kato, S. Hori, T. Saito, K. Suzuki, M. Hirayama, A. Mitsui, M. Yonemura, H. Iba, R. Kanno, *Nat. Energy* **2016**, *1*, 16030.
[6] a) C. Yu, S. Ganapathy, J. Hageman, L. van Eijck, E. R. H. van Eck, L. Zhang, T. Schwietert, S. Basak, E. M. Kelder, M. Wagemaker, *ACS Appl. Mater. Interfaces* **2018**, *10*, 33296–33306; b) N. Minafra, S. P. Culver, T. Krauskopf, A. Senyshyn, W. G. Zeier, *J. Mater. Chem. A* **2018**, *6*, 645–651; c) M. A. Kraft, S. P. Culver, M. Calderon, F. Bocher, T. Krauskopf, A. Senyshyn, C. Dietrich, A. Zevalkink, J. Janek, W. G. Zeier, *J. Am. Chem. Soc.* **2017**, *139*, 10909–10918.
[7] a) Y. Xiao, L. J. Miara, Y. Wang, G. Ceder, *Joule* **2019**, *3*, 1252–1275; b) G. F. Dewald, S. Ohno, M. A. Kraft, R. Koerver, P. Till, N. M. Vargas-Barbosa, J. Janek, W. G. Zeier, *Chem. Mater.* **2019**, *31*, 8328–8337; c) T. T. Zuo, R. Ruess, R. Pan, F. Walther, M. Rohnke, S. Hori, R. Kanno, D. Schroder, J. Janek, *Nat. Commun.* **2021**, *12*, 6669.
[8] a) G. Xu, L. Luo, J. Liang, S. Zhao, R. Yang, C. Wang, T. Yu, L. Wang, W. Xiao, J. Wang, J. Yu, X. Sun, *Nano Energy* **2022**, *92*, 106674; b) L. Zhou, T.-T. Zuo, C. Y. Kwok, S. Y. Kim, A. Assoud, Q. Zhang, J. Janek, L. F. Nazar, *Nat. Energy* **2022**, *7*, 83–93; c) L. Zhou, C.Y. Kwok, A. Shyamsunder, Q. Zhang, X. Wu, L.F. Nazar, *Energy. Environ. Sci.* **2020**, *13*, 2056–2063.
[9] a) X. T. Bai, Y. Duan, W. D. Zhuang, R. Yang, J. T. Wang, *J. Mater. Chem. A* **2020**, *8*, 25663–25686; b) M. Ghidiu, J. Ruhl, S. P. Culver, W. G. Zeier, *J. Mater. Chem. A* **2019**, *7*, 17735–17753.
[10] A. Gautam, M. Sadowski, M. Ghidiu, N. Minafra, A. Senyshyn, K. Albe, W. G. Zeier, *Adv. Energy Mater.* **2021**, *11*, 2003369.
[11] a) P. Adeli, J. D. Bazak, K. H. Park, I. Kochetkov, A. Huq, G. R. Goward, L. F. Nazar, *Angew. Chem. Int. Ed.* **2019**, *58*, 8681–8686; *Angew. Chem.* **2019**, *131*, 8773–8778;b) C. Yu, Y. Li, M. Willans, Y. Zhao, K. R. Adair, F. Zhao, W. Li, S. Deng, J. Liang, M. N. Banis, R. Li, H. Huang, L. Zhang, R. Yang, S. Lu, Y. Huang, X. Sun, *Nano Energy* **2020**, *69*, 104396.
[12] D. H. S. Tan, E. A. Wu, H. Nguyen, Z. Chen, M. A. T. Marple, J.-M. Doux, X. Wang, H. Yang, A. Banerjee, Y. S. Meng, *ACS Energy Lett.* **2019**, *4*, 2418–2427.
[13] F. Walther, R. Koerver, T. Fuchs, S. Ohno, J. Sann, M. Rohnke, W. G. Zeier, J. Janek, *Chem. Mater.* **2019**, *31*, 3745–3755.
[14] A. Schürmann, B. Luerßen, D. Mollenhauer, J. Janek, D. Schröder, *Chem. Rev.* **2021**, *121*, 12445–12464.
[15] F. Strauss, J. H. Teo, J. Maibach, A. Y. Kim, A. Mazilkin, J. Janek, T. Brezesinski, *ACS Appl. Mater. Interfaces* **2020**, *12*, 57146–57154.
[16] a) D. Park, H. Park, Y. Lee, S. O. Kim, H. G. Jung, K. Y. Chung, J. H. Shim, S. Yu, *ACS Appl. Mater. Interfaces* **2020**, *12*, 34806–34814; b) Y. Xiao, Y. Wang, S.-H. Bo, J. C. Kim, L. J. Miara, G. Ceder, *Nat. Rev. Mater.* **2019**, *5*, 105–126; c) J. Auvergniot, A. Cassel, J.-B. Ledeuil, V. Viallet, V. Seznec, R. Dedryvère, *Chem. Mater.* **2017**, *29*, 3883–3890.
[17] F. Walther, S. Randau, Y. Schneider, J. Sann, M. Rohnke, F. H. Richter, W. G. Zeier, J. Janek, *Chem. Mater.* **2020**, *32*, 6123–6136.
[18] a) W. Zhang, F. H. Richter, S. P. Culver, T. Leichtweiss, J. G. Lozano, C. Dietrich, P. G. Bruce, W. G. Zeier, J. Janek, *ACS Appl. Mater. Interfaces* **2018**, *10*, 22226–22236; b) W. Zhang, D. A. Weber, H. Weigand, T. Arlt, I. Manke, D. Schröder, R. Koerver, T. Leichtweiss, P. Hartmann, W. G. Zeier, J. Janek, *ACS Appl. Mater. Interfaces* **2017**, *9*, 17835–17845; c) M. D. Levi, D. Aurbach, *J. Phys. Chem. B* **1997**, *101*, 4630–4640; d) J. Moškon, M. Gaberšček, *J. Power Sources Adv.* **2021**, *7*, 100047; e) J. Moškon, J. Žuntar, S. Drvarič Talian, R. Dominko, M. Gaberšček, *J. Electrochem. Soc.* **2020**, *167*, 140539.
[19] a) G. L. Xu, X. Liu, A. Daali, R. Amine, Z. Chen, K. Amine, *Adv. Funct. Mater.* **2020**, *30*, 2004748; b) F. Strauss, J. H. Teo, A. Schiele, T. Bartsch, T. Hatsukade, P. Hartmann, J. Janek, T. Brezesinski, *ACS Appl. Mater. Interfaces* **2020**, *12*, 20462–20468.
[20] F. Walther, F. Strauss, X. Wu, B. Mogwitz, J. Hertle, J. Sann, M. Rohnke, T. Brezesinski, J. Janek, *Chem. Mater.* **2021**, *33*, 2110–2125.
[21] Y. Yamagishi, H. Morita, Y. Nomura, E. Igaki, *ACS Appl. Mater. Interfaces* **2021**, *13*, 580–586.
[22] a) R. Jung, M. Metzger, F. Maglia, C. Stinner, H. A. Gasteiger, *J. Electrochem. Soc.* **2017**, *164*, A1361–A1377; b) R. Jung, P. Strobl, F. Maglia, C. Stinner, H. A. Gasteiger, *J. Electrochem. Soc.* **2018**, *165*, A2869–A2879; c) T. Bartsch, F. Strauss, T. Hatsukade, A. Schiele, A. Y. Kim, P. Hartmann, J. Janek, T. Brezesinski, *ACS Energy Lett.* **2018**, *3*, 2539–2543.
[23] J. H. Teo, F. Strauss, Đ. Tripković, S. Schweidler, Y. Ma, M. Bianchini, J. Janek, T. Brezesinski, *Cell Rep. Phys. Sci.* **2021**, *2*, 100465.

Manuscript received: September 7, 2022
Accepted manuscript online: November 23, 2022
Version of record online: January 10, 2023